NOTES AND CORRESPONDENCE

Micropulse Lidar Signals: Uncertainty Analysis

ELLSWORTH J. WELTON

Goddard Earth Sciences and Technology Center, University of Maryland, Baltimore County, Baltimore, Maryland

JAMES R. CAMPBELL

Science Systems and Applications, Inc., Lanham, Maryland

2 January 2002 and 10 June 2002

ABSTRACT

Elastic backscatter lidars are used to determine the vertical distribution of cloud and aerosol layers. One such lidar is the micropulse lidar (MPL). A recent paper by Campbell et al. described an algorithm used to process MPL signals. The paper presented procedures that correct for various instrument effects present in the raw signals. The primary instrument effects include afterpulse (detector noise induced from the firing of the laser) and overlap (poor near-range data collection). The outgoing energy of the laser pulses and the statistical uncertainty of the MPL detector must also be correctly determined in order to assess the accuracy of MPL observations. The uncertainties associated with each of these instrument effects, and their contribution to the net uncertainty in corrected MPL signals, were not discussed in the earlier paper. Here in the uncertainties associated with each instrument parameter in the MPL signal are discussed. The uncertainties are propagated through the entire correction process to give a net uncertainty on the final corrected MPL signal. The results show that in the near range, the overlap uncertainty dominates. At altitudes above the overlap region, the dominant source of uncertainty is caused by uncertainty in the pulse energy. However, if the laser energy is low, then during midday, high solar background levels can significantly reduce the signal-to-noise ratio of the detector. In such a case, the statistical uncertainty of the detector count rate becomes dominant at altitudes above the overlap region.

1. Introduction

Micropulse lidar (MPL) systems, as initially described by Spinhirne (1993), are small, autonomous, eye-safe lidars used for continuous observations of the vertical distribution of cloud and aerosol layers (see also Spinhirne et al. 1995a,b). The MPL was initially developed for work within the Atmospheric Radiation Measurement (ARM) Program (Stokes and Schwartz 1994) but has since been used in several independent field experiments around the world (Welton et al. 2000, 2002; Peppler et al. 2000; Voss et al. 2001). An overview of the MPL instruments operated within the ARM Program is discussed by Campbell et al. (2002), henceforth referred to as CA.

Welton et al. (2000) and CA discuss the nature of the measured MPL signal with respect to the lidar equation (Fernald et al. 1972). The measured signals are shown to differ from the theoretical lidar equation because of instrument effects. Both Welton et al. and CA develop correction factors for each instrument-related effect, and present algorithms that convert the measured signal into a form that complies with the lidar equation.

The two algorithms differ in their approach to the correction process. The earlier algorithm by Welton et al. determined the correction factors by forcing measured signals to conform to a modeled lidar signal containing only molecular scattering. However, this method is only useful when measurements can be conducted in regions free of aerosols and clouds, as from atop mountains. The CA algorithm is not dependent upon this condition and is more applicable to most field conditions. Also, the CA algorithm is more rigorous in its construction and better suited to understanding the uncertainties involved in the correction process. For these reasons, an adapted version of the CA algorithm was used by Welton et al. (2002) for processing MPL data from a later field experiment.

The authors intend to utilize the CA algorithm for future studies. However, CA did not discuss the uncer-

Corresponding author address: Dr. Ellsworth J. Welton, Goddard Earth Sciences and Technology Center, University of Maryland, Baltimore County, Baltimore, MD 21250.
E-mail: welton@virl.gsfc.nasa.gov

tainties associated with the MPL instrument parameters or the net uncertainty associated with their correction technique. This research note presents a study of the uncertainties associated with the correction factors discussed by CA. The uncertainties are propagated through the CA algorithm to yield a net uncertainty in the final corrected MPL signal.

2. The MPL signal

This section describes the terms that are present in the lidar equation. The raw MPL count rate is presented as Eq. (2) in CA, and is rewritten here as

$$P_{\text{raw}}(r) = \frac{CEO(r)[\beta_M(r) + \beta_P(r)]T_M^2(r)T_P^2(r)}{D(P_{\text{raw}})r^2} + \frac{A_{\text{raw}}(r, E)}{D(P_{\text{raw}})} + \frac{B_{\text{raw}}}{D(P_{\text{raw}})}, \quad (1)$$

where $P_{\text{raw}}(r)$ is the measured signal (photoelectrons/microseconds per shot) at range r, C is a calibration value, E is the pulse energy (μJ), $D(P_{\text{raw}})$ is the detector dead-time factor, $O(r)$ is the overlap function, $A(r, E)$ is the detector afterpulse (photoelectrons/microseconds per shot), and B is the solar background signal (photoelectrons/microseconds per shot). The backscatter cross-section terms, $\beta_M(r)$ and $\beta_P(r)$, in Eq. (1) are due to molecules and particles, respectively. Sources of particle backscatter include clouds and aerosols, or a mixture of both. The transmission terms, $T_M^2(r)$ and $T_P^2(r)$, are given by

$$T_i^2(r) = \exp\left[-2\int_0^r \sigma_i(r')\,dr'\right], \quad (2)$$

where $\sigma(r)$ is the extinction coefficient, and the i subscript denotes either a molecular or particle quantity. The integral of the extinction coefficient from the MPL to any range is the optical depth over that distance. The transmission terms are squared to account for the two-way path of the laser pulses.

The aim of the CA correction algorithm is to remove all instrument parameters from Eq. (1) except C, and to subtract B. The signal resulting from the correction process is called the normalized-relative-backscatter (NRB) signal. The NRB signal, $P_{\text{NRB}}(r)$, is defined as

$$P_{\text{NRB}}(r) = C[\beta_M(r) + \beta_P(r)]T_M^2(r)T_P^2(r). \quad (3)$$

CA derives the NRB equation in terms of the raw signal parameters [see Eq. (4) in CA]. The NRB signal is significant because it is dependent on atmospheric parameters and only one instrument parameter, C. The NRB signals are used to provide information on the vertical structure of aerosols and clouds, and also to solve for particulate extinction profiles (Welton et al. 2000, 2002).

3. NRB signal uncertainties

Knowledge of the uncertainty in the NRB signals is required to assess the accuracy of aerosol and cloud heights identified from the signals, as well as extinction profiles calculated from them. Using Eq. (4) from CA, the net uncertainty in the NRB signal, $\delta P_{\text{NRB}}(r)$, is given by

$$\delta P_{\text{NRB}}(r) = P_{\text{NRB}}(r)\sqrt{\frac{[\delta P(r)]^2 + \delta B^2 + [\delta A_{\text{raw}}(r, E)]^2}{[P(r) - B - A_{\text{raw}}(r, E)]^2} + \left[\frac{\delta E}{E}\right]^2 + \left[\frac{\delta O(r)}{O(r)}\right]^2}, \quad (4)$$

where $\delta P(r)$ is the uncertainty in the raw signal, δB is the uncertainty in the background, $\delta A_{\text{raw}}(r, E)$ is the uncertainty in the measurement of the afterpulse, δE is the uncertainty associated with measuring the outgoing energy, and $\delta O(r)$ is the uncertainty in the determination of the MPL overlap function. Each of these uncertainty terms is discussed in detail in the following sections.

a. *Uncertainty in the raw signal and measured background*

Using Poisson statistics, the uncertainty in $P(r)$ is

$$\delta P(r) = \sqrt{\frac{P(r)}{N}}, \quad (5)$$

where N is the number of shots during the acquisition of the signal and is dependent on the data rate. The value of N is typically either 75 000 for a 30-s data rate or 150 000 for a 1-min data rate. The uncertainty in B is also given by the form of Eq. (5) but is done using the signal returns from 45 to 55 km as discussed by CA.

The correction of detector dead-time effects could also factor into the uncertainties in $P(r)$ and B. Dead-time effects are caused by saturation of the detector signals at high count rates and are discussed in detail by CA. Here we attempt to quantify the uncertainty in the dead-time correction based on information provided by the manufacturer and others with expertise in the field of photon counting detectors (X. Sun 2001, personal communication).

The dead-time factor is determined using the following equation:

$$D(P_{\text{raw}}) = \frac{\chi}{P_{\text{raw}}A}, \quad (6)$$

where χ is a calibrated source signal, A is the total attenuation of the optical path from the source to the

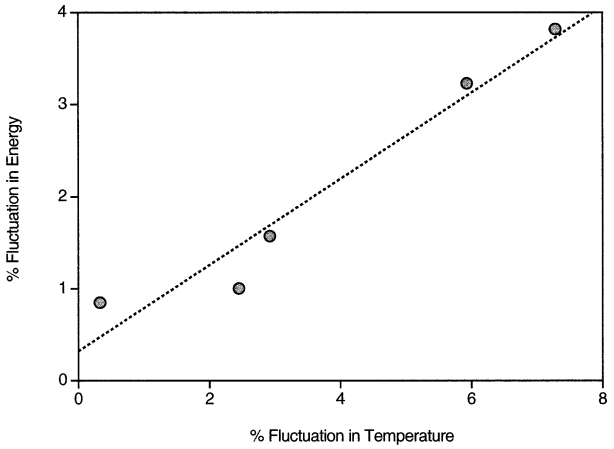

FIG. 1. Percent fluctuation in energy monitor values vs the percent fluctuation in temperature for five different MPL systems. The mean length of time for these measurements was approximately 23 h.

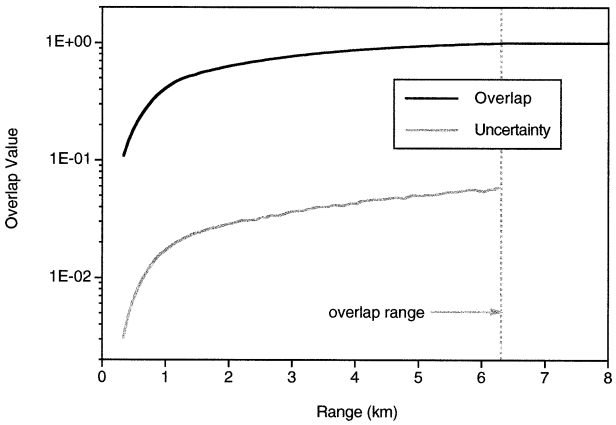

FIG. 2. A typical overlap function and its uncertainty.

detector, and P_{raw} is the observed photon count rate. The uncertainty in $D(P_{\text{raw}})$ is given by

$$\delta D(P_{\text{raw}}) = D(P_{\text{raw}}) \sqrt{\left(\frac{\delta\chi}{\chi}\right)^2 + \left(\frac{\delta A}{A}\right)^2 + \left(\frac{\delta P_{\text{raw}}}{P_{\text{raw}}}\right)^2}, \quad (7)$$

where $\delta\chi$ and δP_{raw} are the uncertainties in the source and measured signals, respectively, determined using Poisson statistics, and δA is the uncertainty in the attenuation term. The uncertainties in each signal term are estimated assuming a per-second count rate with no time average. The source uncertainty was well below 1% and was negligible. The attenuation uncertainty was ignored in order to assess the uncertainty in the dead time caused by fluctuations in the source and measured signal.

The dead-time uncertainty was found to be negligible at high count rates but approaches 1% at low count rates because the detector uncertainty is highest when the count rate is low. However, the dead-time factor itself is only significant for values above 1.01, the level at which the measured signals are affected by at least 1% due to dead-time effects. At dead-time factors above 1.01, the dead-time uncertainty is less than 0.3%. As a result, the source and measured signal uncertainties contribute very little to the overall dead-time uncertainty. Instead, the uncertainty in the dead-time factor is dependent almost entirely on the uncertainty in the attenuation optic. The attenuation uncertainty is not known at this time. For the purposes of this study, we will consider this to be small and the overall dead-time uncertainty to be negligible.

b. Uncertainties in the laser energy

As discussed by CA, a portion of the outgoing laser pulse energy is measured in real time by another detector, the energy monitor. Changes in the energy monitor value from pulse to pulse during the measurement period will produce uncertainty in the energy value. If the energy uncertainty becomes high it can dominate the uncertainty in the MPL signal. Therefore, the energy monitor value must be carefully considered.

The energy monitor value can change from pulse to pulse due to changes in the laser power setting, degradation of the laser diode over time, changes in beam quality output from the laser head, and statistical fluctuations in the energy monitor. The laser power setting is fixed during operation of the MPL. Therefore, the diode power will only drop if the laser system begins to degrade; however, this takes place over a long time span and will not produce pulse-to-pulse changes in the energy unless a catastrophic failure occurs. The laser head components may also degrade with time, but, again, this will not produce significant pulse-to-pulse changes unless the laser head breaks. The beam quality may be affected by environmental changes such as increase or decrease in temperature and humidity of the laser components. This could occur over much smaller time frames and is considered a possible source of uncertainty. Statistical fluctuations in the energy monitor are also considered a source of uncertainty. In addition, temperature changes on the energy monitor produce another source of uncertainty because of thermal noise in the detector.

The uncertainty in the energy monitor value was determined using the following procedure. Data from five MPL systems were collected. The average energy, percent energy fluctuation, average temperature, and percent temperature fluctuation of each MPL system over long time periods was measured. The energy monitor values ranged from 3.71 to 7.64 μJ, and the temperature values ranged from 26.93° to 30.55°C between the MPL systems picked for this study. MPL systems have varying degrees of laser quality due to age, and this range of energy covers the typical span found in most MPL systems. Also, the temperature range covers the typical span encountered during most MPL operations. Figure 1 shows the percent fluctuation in energy versus the percent fluctuation in temperature for the five MPL systems. The data show that when the change in temper-

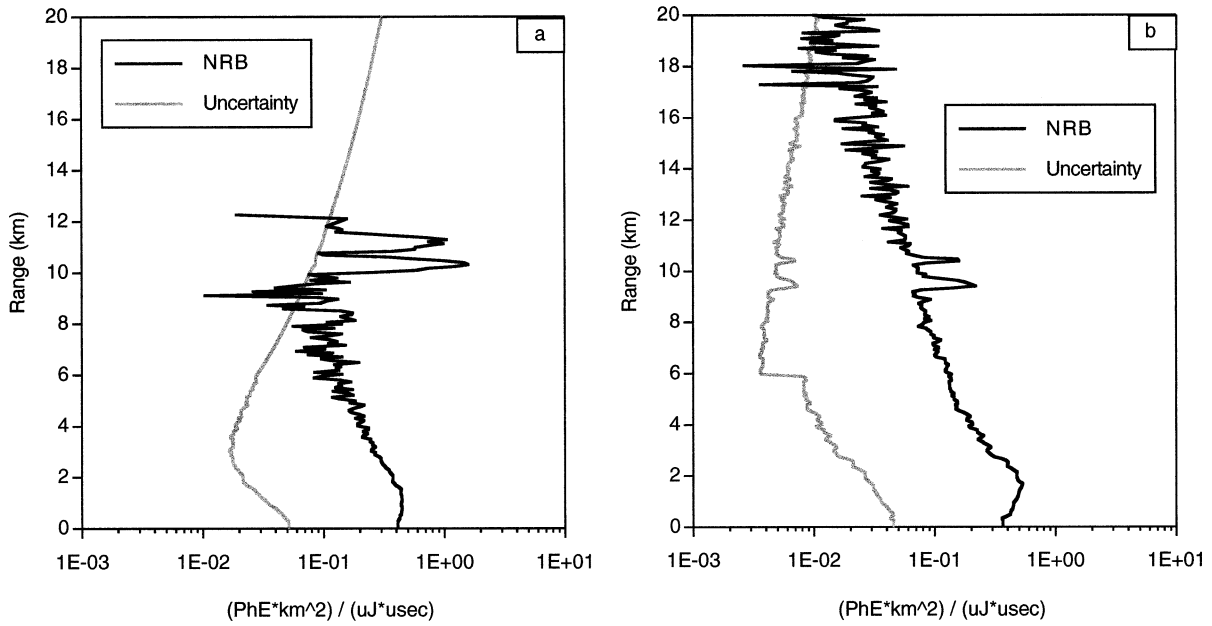

FIG. 3. Examples of NRB signals acquired during (a) daytime and (b) nighttime. Corresponding uncertainties are also shown.

ature is low, the percent fluctuation in the energy monitor value is approximately 1% or less. When the change in temperature is low, the primary source of energy change is simply statistical fluctuation within the detector. Typical MPL data acquisition rates are 1 min or less, and temperature changes are negligible over such short time spans unless there is a noticeable problem with the instrument. Therefore, under normal conditions the uncertainty in the energy monitor value is assumed to be 1%. However, if the data rate is increased to several minutes or more, then temperature fluctuations affecting the energy uncertainty should be considered.

c. Uncertainty in the afterpulse correction

A complete discussion of afterpulse is given by CA, so only a brief description is given here. The initial firing of each laser pulse impacts the detector because the MPL shares the same transmit and receive path. The initial pulse on the detector is large and creates a false signal that must be removed from the measured signals by predetermining $A_{\text{raw}}(r, E)$ and then subtracting it from $P(r)$. Afterpulse is determined by covering the MPL and preventing signals from being transmitted. In this arrangement, the detector only measures the afterpulse signal and background, which is equal to the detector dark noise with the lid on. The afterpulse is dependent upon the output energy and is given by Eq. (6) in CA, rewritten here as

$$A_{\text{raw}}(r, E_A) = E_A A_N(r), \tag{8}$$

where E_A is the energy monitor value during the afterpulse measurement, and $A_N(r)$ is equal to $n'_{\text{ap}}[r]/E_o$ using the form of CA.

Here $A_N(r)$ is referred to as the normalized afterpulse. In order to measure $A_N(r)$, the dark noise is subtracted from $P(r)$ and the result is divided by E_A; $A_N(r)$ is the average of the signals over the afterpulse measurement period (several minutes), and the normalized afterpulse uncertainty, $\delta A_N(r)$, is

$$\delta A_N(r) = A_N(r)\sqrt{\frac{\delta P(r)^2}{[P(r) - B]^2} + \left(\frac{\delta E_A}{E_A}\right)^2}, \tag{9}$$

where δE_A is the uncertainty in the outgoing energy during the afterpulse measurement. The afterpulse measurement is performed over a period of several minutes; therefore one cannot assume that the energy uncertainty is 1% (as during normal operation of the lidar). Therefore, the energy uncertainty is determined by using the standard deviation of the energy values throughout the measurement period. Data show that the first term under the square root on the rhs of Eq. (9) is negligible compared to the energy term; therefore the normalized afterpulse uncertainty can be approximated by the uncertainty in the energy value during the measurement period (typically less than 5%).

Signals measured during regular operations are corrected by subtracting $EA_N(r)$ from $[P(r) - B]$ and then dividing by E. However, B and E are the values taken during the regular measurement, not the afterpulse measurement. Therefore, the raw afterpulse uncertainty, $\delta A_{\text{raw}}(r, E)$, is required and is given by

$$[\delta A_{\text{raw}}(r, E)]^2 = [A_N(r)\delta E]^2 + [E\delta A_N(r)]^2, \tag{10}$$

[see Eq. (4)].

d. Uncertainty in the overlap correction

The next step in MPL processing is the overlap correction. A complete discussion of overlap is given by

CA, so only a brief description is given here. The overlap function accounts for signal loss in the near range due to poor receiver efficiency of the telescope and associated optics in this region. The overlap problem must be corrected in order to analyze boundary layer aerosols. The CA overlap correction process involves acquiring MPL data while the instrument is oriented horizontally. In this arrangement, both β and σ are assumed to be constant with range. Using Eqs. (8) and (9) from CA, the horizontal MPL signal, $P_H(r)$, is given by

$$\ln[P_H(r)] = \ln[C\beta] + \ln[O(r)] - 2\sigma r, \quad (11)$$

where $P_H(r)$ has been energy normalized and afterpulse corrected. At distances greater than the overlap range, $O(r)$ is equal to one, and the second term on the rhs of Eq. (11) is zero. In this region, $\ln[P_H(r)]$ is linear with respect to range. A least squares linear fit is applied to N data points in the fit region discussed by CA. The resulting linear fit is given by

$$\ln[P_F(r)] = \ln[C\beta] - 2\sigma r, \quad (12)$$

where the y intercept is $\ln[C\beta]$, and the slope is -2σ. The overlap function is calculated using the following equation:

$$O(r) = \begin{cases} \dfrac{P_H(r)}{P_F(r)} & r < r_o \\ 1 & r \geq r_o, \end{cases} \quad (13)$$

where r_o is the overlap range, and $P_F(r)$ is simply the exponential of the fit line. The uncertainty in the overlap is given by

$$\delta O(r) = O(r)\sqrt{\left[\frac{\delta P_H(r)}{P_H(r)}\right]^2 + \left[\frac{\delta P_F(r)}{P_F(r)}\right]^2}. \quad (14)$$

The first term under the square root in Eq. (14) is uncertainty in the signal and is given by

$$\left[\frac{\delta P_H(r)}{P_H(r)}\right]^2 = \frac{[\delta P(r)]^2 + \delta B^2 + [A_N(r)\delta E_o]^2 + [E_o \delta A_N(r)]^2}{[P(r) - B - E_o A_N(r)]^2} + \left[\frac{\delta E_o}{E_o}\right]^2, \quad (15)$$

where E_o is the energy monitor value during the overlap measurement. The second term under the square root in Eq. (14) is uncertainty due to the fit process and is given by

$$\left[\frac{\delta P_F(r)}{P_F(r)}\right]^2 = \left[\frac{\delta(C\beta)}{C\beta}\right]^2 + \left[\frac{\delta(\exp[-2\sigma r])}{\exp[-2\sigma r]}\right]^2. \quad (16)$$

The fit uncertainty is a function of the uncertainties in both the y intercept and slope obtained during the fit. Standard error analysis is used to determine the uncertainties for both parameters. First we define the following terms:

$$\Omega = X\sum_{i=1}^{X} r_i^2 - \left(\sum_{i=1}^{X} r_i\right)^2 \quad \text{and} \quad (17)$$

$$s^2 = \frac{1}{X-2}\sum_{i=1}^{X}\{\ln[P_H(r)] - \ln[P_F(r)]\}^2. \quad (18)$$

The uncertainty in the y intercept is then given by

$$\delta[\ln(C\beta)] = \sqrt{\frac{s^2}{\Omega}\sum_{i=1}^{X} r_i^2}, \quad (19)$$

and the uncertainty in the slope is

$$\delta(-2\sigma) = \sqrt{X\frac{s^2}{\Omega}}. \quad (20)$$

The results of Eqs. (19) and (20) are then used to determine the uncertainty terms on the rhs of Eq. (16). The equations are given by

$$\frac{\delta(C\beta)}{C\beta} = \frac{\{e^{\ln[C\beta]+\delta(\ln[C\beta])} - e^{\ln[C\beta]}) + (e^{\ln[C\beta]} - e^{\ln[C\beta]-\delta(\ln[C\beta])})\}}{2e^{\ln[C\beta]}} \quad \text{and} \quad (21)$$

$$\frac{\delta\{\exp[-2\sigma r]\}}{\exp[-2\sigma r]} = r\delta(-2\sigma). \quad (22)$$

The final overlap uncertainty is calculated using Eq. (14). Figure 2 shows a typical overlap function and its uncertainty.

4. Example of uncertainty in MPL signals

Figure 3 shows examples of NRB signals acquired during (a) daytime and (b) nighttime at typical MPL data rates (1 min). The uncertainties in each signal (10–12 km) are also shown. The boundary layer and cirrus clouds are visible in both plots. The nighttime uncertainty is less than the daytime because of the lack of solar background at night. Also, the daytime signal fluctuated around zero above the cloud in Figure 3a and was not plotted because a log scale was used. The uncertainty is shown to become equal to, and surpass, the

signal strength at this altitude, which indicates that the algorithm presented here is correctly representing uncertainty in the measured signals.

Despite higher uncertainties during daytime, the MPL is able to detect the presence of cirrus layers at a 1-min data rate. During the daytime, signal uncertainty approaches 100% near 8 km in the clear-air region. However, when cirrus is encountered the NRB signal strength increases, becoming far higher than the uncertainty. This illustrates how the MPL is able to detect clouds even in regions where the signal uncertainty becomes very high. However, detecting thin cirrus (or weak aerosol layers) during daytime at 1-min data rates is still a difficult task. This problem can be overcome by averaging NRB signals over periods of several minutes.

5. Conclusions

Procedures to determine the uncertainty in NRB signals obtained with MPL systems have been presented. The procedures were shown to produce realistic uncertainties for a sample dataset. The sources of uncertainty in the NRB signals were identified. In general, near the surface the overlap uncertainty is the dominant source of uncertainty in the NRB signal. At altitudes above the overlap region, the dominant source of uncertainty in the NRB signal is typically due to uncertainty in the energy. However, during daytime B increases and reduces the signal-to-noise ratio, which causes $\delta P_{\mathrm{NRB}}(r)$ to increase accordingly. Therefore, during the daytime B is also a large source of uncertainty at higher altitudes. As a result, longer time averages may be needed to detect thin cirrus and high-altitude aerosol layers during the daytime.

Acknowledgments. This work was conducted by members of the MPLNET project at NASA Goddard Space Flight Center. The MPLNET project is funded by the NASA Earth Observing System and the NASA SIMBIOS project. The authors thank Stan Scott, Tim Berkoff, Matt McGill, Dennis Hlavka, Bill Hart, Jim Spinhirne, and Xiaoli Sun for helpful discussions on the matter of uncertainties in the various MPL components.

REFERENCES

Campbell, J. R., D. L. Hlavka, E. J. Welton, C. J. Flynn, D. D. Turner, J. D. Spinhirne, V. S. Scott, and I. H. Hwang, 2002: Full-time, eye-safe cloud and aerosol lidar observation at Atmospheric Radiation Measurement Program sites: Instrument and data processing. *J. Atmos. Oceanic Technol.,* **19,** 431–442.

Fernald, F. G., B. M. Herman, and J. A. Reagan, 1972: Determination of aerosol height distributions by lidar. *J. Appl. Meteor.*, **11,** 482–489.

Peppler, R. A., and Coauthors, 2000: ARM Southern Great Plains site observations of the smoke pall associated with the 1998 Central American fires. *Bull. Amer. Meteor. Soc.,* **81,** 2563–2591.

Spinhirne, J. D., 1993: Micro pulse lidar. *IEEE Trans. Geosci. Remote Sens.,* **31,** 48–55.

——, J. A. R. Rall, and V. S. Scott, 1995a: Compact eye-safe lidar systems. *Rev. Laser Eng.,* **23,** 112–118.

——, ——, and ——, 1995b: Compact eye-safe lidar systems. *Rev. Laser Eng.,* **23,** 26–32.

Stokes, G. M., and S. E. Schwartz, 1994: The Atmospheric Radiation Measurement (ARM) Program: Programmatic background and design of the cloud and radiation testbed. *Bull. Amer. Meteor. Soc.,* **75,** 1201–1221.

Voss, K. J., E. J. Welton, P. K. Quinn, J. Johnson, A. Thompson, and H. Gordon, 2001: Lidar measurements during Aerosols99. *J. Geophys. Res.,* **106,** 20 821–20 832.

Welton, E. J., and Coauthors, 2000: Ground-based lidar measurements of aerosols during ACE-2: Instrument description, results, and comparisons with other ground-based and airborne measurements. *Tellus,* **52B,** 635–650.

——, and Coauthors, 2002: Measurements of aerosol vertical profiles and optical properties during INDOEX 1999 using micro-pulse lidars. *J. Geophys. Res.,* in press.